Highlights

Reverse-Time Migration for Evaluating the Internal Structure of Tree-Trunks Using Ground-Penetrating Radar

- A processing framework for detecting tree decays in diseased trees.
- A real-field case study that demonstrates the capabilities of the suggested method.

Reverse-Time Migration for Evaluating the Internal Structure of Tree-Trunks Using Ground-Penetrating Radar

Amir M. Alani[1], Iraklis Giannakis[2], Lilong Zou[3], Livia Lantini[4] and Fabio Tosti[5]

[1] University of West London, School of Computing and Engineering, St Mary's Rd, Ealing, London W5 5RF. E-mail: amir.alani@uwl.ac.uk

[2] University of West London, School of Computing and Engineering, St Mary's Rd, Ealing, London W5 5RF. E-mail: iraklis.giannakis@uwl.ac.uk

[3] University of West London, School of Computing and Engineering, St Mary's Rd, Ealing, London W5 5RF. E-mail: lilong.zou@uwl.ac.uk

[4] University of West London, School of Computing and Engineering, St Mary's Rd, Ealing, London W5 5RF. E-mail: livia.lantini@uwl.ac.uk

[5] University of West London, School of Computing and Engineering, St Mary's Rd, Ealing, London W5 5RF. E-mail: fabio.tosti@uwl.ac.uk

 Corresponding author: Iraklis Giannakis

E-mail: iraklis.giannakis@uwl.ac.uk

48 **Abstract:**

49 Modern socioeconomic factors such as global timber trade and international

50 travelling have contributed to the rapid increase of Emerging Infectious Diseases

51 (EIDs) of trees with devastating effects to the European forests and woodlands.

52 To that extent, numerous non-destructive methodologies have been suggested as

53 diagnostic tools in order to effectively monitor and maintain potential outbreaks.

54 Ground-penetrating radar (GPR) is an appealing method for tree monitoring as it

55 provides with a trivially deployable and efficient detection tool, suitable for

56 large-scale forestry applications. Nonetheless, traditional GPR approaches are

57 tuned for surface measurements and they are not compatible with the unique

58 measurement configurations associated with forestry applications. Within that

59 context, we present a novel-processing framework, which is capable

60 of addressing features with irregular measurements on closed surfaces. A

61 positioning method is described that exploits a wheel-measuring device in order

62 to accurately associate each A-Scan with its corresponding coordinates. In

63 addition, a processing pipeline is presented that aims at eliminating the ringing

64 noise due to the layered nature of the trees. Lastly, a reverse-time migration is

65 applied to the processed B-Scan in order to effectively map the reflectors present

66 within the trunk. The suggested scheme is successfully tested in both numerical

67 and real-field experiments, indicating the validity of the current approach.

68

1. Introduction

70

71 Emerging Infectious Diseases (EIDs) of trees -caused by pathogens, pests and

72 fungi- pose a major threat for forests and woodlands [1], [2]. Recent outbreaks

73 almost brought some species to extinction [3], [4] with devastating effects to the

74   European flora. It should be highlighted that from 1995-2010, a 13-fold increase

75   of EIDs has been recorded globally [2]. This rapid increase is due to anthropic

76   activities such as international travelling [2], global timber trade [1] and human

77   population increase [5]. Furthermore, climate change and the consequent rise of

78   the global temperature have added to this phenomenon [2].

79   Representative examples of recent outbreaks of EIDs are the ash dieback, the

80   acute oak decline (AOD) and the chestnut blight. Ash dieback is a prominent EID

81   that has invaded the United Kingdom (UK) in 2012 [1] and it has spread majorly

82   in central England and Wales [6]. Less than 5% of the ash trees are immune to

83   this disease and it is predicted that most of the ash trees in the UK are going to be

84   affected and die in the next twenty years [7]. AOD is a particularly aggressive

85   EID that can lead to tree mortality within a period of 3-5 years [8]. AOD has been

86   introduced to the UK in 2006 and since then has rapidly spread mostly in the

87   central part of England [9]. The effects of ash dieback and AOD to the forests and

88   woodlands of the UK resemblance the effects of chestnut blight to the chestnut

89   population in the North America during the last century [10]. Chestnut blight

90   accidentally invaded North America in 1904 and rapidly spread within the

91   following 40 years [10]. The nearly four billion chestnut population of North

92   America almost brought to extinction with just small populations surviving in

93   the Pacific Northwest [10].

94   Tree decays and compartmentalisation of decays are robust diagnostic criteria

95   for EIDs [11] Due to the importance of decays to the overall health status of a

96   tree, numerous drilling approaches have been suggested for assessing the

97   internal structure of trees and detecting hidden cavities [12], [13]. Although

98   drilling methods are accurate and reliable, nonetheless, destructive techniques

99   can cause irreversible damage to the tree, making it more vulnerable to fungi,

100   pathogens and pests. In addition, drilling methods are constrained to a single

101   point and fail to provide a coherent and comprehensive image of the internal

102   structure of the trunk. Within that context, there is an on-going call for novel

103   detection approaches and modern diagnostic tools [2], capable of detecting early

104   decay in an efficient and practical manner.

105   Non-destructive testing (NDT) for wood monitoring [14] is a suitable candidate

106   for detecting early decays in tree-trunks and their components (e.g., tree roots

107   [15], [16], [15]). NDT provides with a robust set of tools that can map the

108   internal structure of trees without disturbing its layers. The most mainstream

109   amongst the NDT techniques -applied for forestry applications- is the electrical

110   resistivity [16] and the ultrasound tomography [17]. Both of these methods can

111   effectively assess the health condition of a tree. Nonetheless, the measurement

112   configurations of these techniques make them unattainable for large-scale

113   forestry applications in which numerous trees have to be assessed in a short

114   period of time.

115   To tackle this, common-offset (CO) ground-penetrating radar (GPR) has been

116   suggested as an efficient and practical approach for tree monitoring [18]. To that

117   extent, a technique based on the interpretation of B-Scans in polar coordinates is

118   described in [19], [20], a layer-based detection is presented in [21] and a

119   hyperbola fitting approach is discussed in [18]. Apart from signal processing

120   approaches, tomographic methods are particularly appealing for tree monitoring

121   applications due to the fact that the measurements are taken on a closed surface

122   using a dense configuration. Microwave tomography tuned for cylindrical host

123   media has been extensively applied for column investigations [22] and

124 biomedical applications [23]. Furthermore, tomographic approaches based on

125 the Born approximation and subject to CO-GPR configurations have shown

126 promising results when applied for tree monitoring and early decay detection

127 [24]. However, the resulting image may still be corrupted by artefacts,

128 decreasing the signal-to-clutter ratio and reducing the reliability of the final

129 results [24].

130 Migration is a mainstream processing tool that has been applied for both

131 seismic and GPR applications in an effort to focus the received signal and

132 increase the overall signal-to-clutter ratio [25]. The minimum computational

133 requirements combined with its accuracy, have made migration one of the most

134 extensively used approaches amongst GPR practitioners with a wide range of

135 applications ranging from landmine detection [26], [27] to topography mapping

136 [28]. Regarding forestry applications, a hyperbola summation -that

137 resemblances Kirchhoff migration- has been suggested for tree measurements in

138 [29]. In contrast to typical migration schemes applied to GPR [25], the approach

139 described in [29] is not constrained to clinical half-spaces and thus, it can be

140 applied in a straightforward manner to any arbitrary topography. Although

141 preliminary laboratory results are promising [29], nonetheless real-field case

142 studies are necessary in order to provide concrete evidences regarding the

143 applicability of GPR for decay detection.

144

145 *1.1 Statement of the Problem*

146 CO-GPR has the potential to answer the on-going call for the modernization of

147 detection tools for arboriculture applications. In order for GPR to be established

148 as a mainstream forestry tool, processing methods have to be fine-tuned

149 accordingly and subsequently be subjected to a rigorous validation process. To

150 that extent, numerical models and laboratory experiments can provide useful

151 insights on the accuracy and efficiency of each investigated technique.

152 Nonetheless, numerical and laboratory data can widely deviate from real field

153 case studies and thus lead to an overestimation of the capabilities of GPR. Real-

154 field case studies, although essential, are often unattainable due to practical

155 considerations. In particular, a proper arboriculture case study should involve a

156 diseased tree that is going to be cut down after the completion of the

157 measurements. Furthermore, the fallen tree has to be cut into several slices in

158 order to get an insight on its internal structure for validation purposes. The

159 aforementioned procedure requires a dedicated and properly trained group of

160 foresters that is often not available.

161

162 *1.2 Aims and Objectives*

163   In the current paper, we present a more efficient and less time-consuming

164 focusing approach (compared to [29]) that is based on reverse-time (RT)

165 migration [30]. In particular, the method described in [29] is a hyperbola

166 summation that requires extensive 2D interpolations within the B-Scan. This

167 results to large computational requirements especially when applied to 3D

168 measurements. RT migration is particularly appealing for tree measurements

169 due to its minimum computational requirements and its flexibility when it comes

170 to rough topography. The most computationally intensive part of RT migration is

171 an inverse fast Fourier transform which, can be executed in real-time in typical

172 computers. The suggested scheme is successfully validated using both synthetic

173 data and a real-field case study that involves a diseased urban tree within the

174   greater London area, UK. The proposed methodology was proven capable of

175   detecting decay of various sizes within the resolution of the employed antenna.

176   The current case study provides concrete evidences that GPR has the potential to

177   become an efficient tool for forestry and arboriculture applications.

178   The paper is organised as follows. Section 2 describes the theoretical

179   background of the RT migration as well as the processing pipeline that was

180   preliminarily employed. In addition to this, the positioning framework suggested

181   in [15] is discussed for the sake of consistency with presented results. Section 3

182   presents the numerical and real-field case studies accompanied with a detailed

183   discussion on the results. Lastly, the conclusions are drawn in Section 4.

184   **2. Methodology**

185

186   The proposed methodology consists of four distinct stages, namely, A) data

187   positioning, B) pre-processing, C) migration and D) post-migration smoothing

188   (see Figure 1). In the first step, the measurements are positioned along the

189   surface of the trunk using an arc length parameterization. Subsequently the raw

190   data are processed in order to eliminate unwanted clutter and ringing noise. The

191   first two steps are not sequential and thus the order can be reversed. The

192   processed B-Scan is then migrated. Lastly, a smoothing filter is applied in order

193   to eliminate migration artefacts. Notice that all the aforementioned steps require

194   minimum computational requirements and can be executed in almost real-time

195   using conventional mainstream computers.
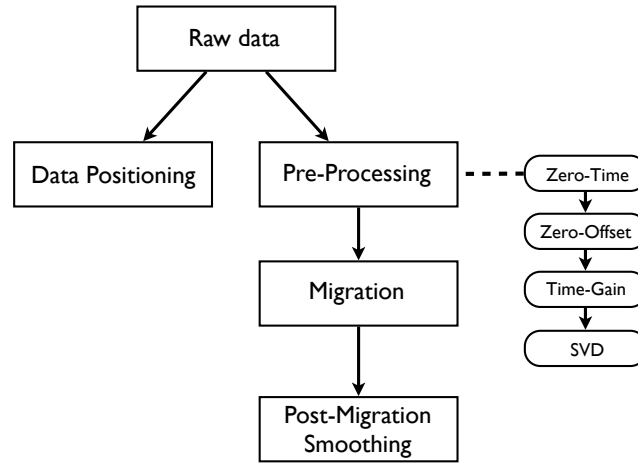
Figure 1: Flowchart describing the proposed processing framework.

198   *2.1 Positioning Scheme*

199   Typical CO-GPR systems position each A-Scan based on a wheel-measuring

200   device that associates every received signal output with its associate position.

201   This configuration was designed for line measurements subject to flat surfaces

202   and fails to compensate for irregular topographies. Regarding tree surveys, it is

203   known that measurements are collected on a highly irregular surface. Thus, prior

204   to any processing approach, each A-Scan should be accurately positioned along

205   the investigated surface. To that extent, in order to convert the measured

206   distance (from the wheel-measuring device) to its corresponding coordinates,

207   we employ an arc-length parameterisation [31], [32], initially described in [18].

208   The first step of the arc-length parameterisation is to digitize the investigated

209   surface using a sufficient (*n*) number of points along the surface of the trunk

210    $\mathbf{x}, \mathbf{y} \in \mathbb{R}^n$. Subsequently, the vector $\mathbf{t} \in \mathbb{R}^n \mid 0 < t < 1$ is defined, which is going to

211   be used for the parametric representation of the shape of the tree [18]. A spline

212   interpolation is subsequently used in order to map the vectors $(\mathbf{x}, \mathbf{t})$ and $(\mathbf{y}, \mathbf{t})$ to

213   the continuous scalar functions $P(t)$ and $Q(t)$ respectively. Notice that the bounds

214   of **t** do not affect the final output since the coefficients of the fitted polynomial

9

215   are adjusted accordingly. The position vector $\mathbf{F} = [P(t), Q(t)]$ represents the shape

216   of the tree with respect to the arbitrary value t. The arc-length (s) of the

217   positional vector $\mathbf{F}$ throughout the vector $\mathbf{t}$ is given by

$$s(\tau) = \int_0^\tau ||\frac{d\mathbf{F}}{dt}||dt = \int_0^\tau \sqrt{\left(\frac{dP(t)}{dt}\right)^2 + \left(\frac{dQ(t)}{dt}\right)^2} dt \quad . \quad (1)$$

219   where $\tau \in [0, 1]$ is a continuous variable along the boundaries of the arbitrary

220   vector $\mathbf{t}$. The integral in (1) is evaluated numerically [15] using different τ values

221   varying from [0,1]. A spline interpolation is then used in order to map the values

222   of τ with respect to the distance s. Thus, the distance can now be expressed in a

223   continuous manner with respect to t. Consequently; the position vector can now

224   be expressed with respect to the distance $\mathbf{F} = [P(t(s)), Q(t(s))]$. This implies that

225   the position of the antenna can now be calculated based on the distance (s)

226   measured using a typical wheel-measuring device [18].

227

228   *2.2 Pre-Processing*

229   Prior to the RT migration, the raw B-Scan has to be carefully processed in order

230   to transform the data in a suitable format for the following processing stages.

231   The processing pipeline applied in this paper -similar to [18]- consists of four

232   sequential steps:

233   • *Time-zero removal:* in this step, the starting time t_0 of the pulse is

234   estimated and the signal prior to t_0 is deleted. This step is particularly

235   important since the estimated time-zero greatly affects the performance

236   of the RT migration. The first peak of the derivative of the A-Scan with

237   respect to time is chosen to represent the time-zero in the current paper.

- 238 • *Zero-offset removal:* in this step, static phenomena that corrupt the
- 239 received A-Scans are removed by fitting a second order polynomial to
- 240 the received signal [33].

- 241 • *Time-varying gain:* an incremental gain is applied in order to compensate
- 242 for the losses present within the trunk.

- 243 • *Singular value decomposition:* trees are complex media that consist of
- 244 distinct layers with different compositions and dielectric properties [18].
- 245 Due to the layered nature of trees, the raw B-Scan is corrupted with
- 246 ringing noise that masks the reflections from the decay and reduces the
- 247 overall signal-to-clutter ratio [18]. To tackle this, a singular value
- 248 decomposition (SVD) filter (similar to [18]) is applied here. The raw B-
- 249 Scan is treated as a 2D matrix $\mathbf{B} \in \mathbb{R}^{w \times v}$ where w and v are the number of
- 250 measurements and the number of time-steps, respectively. The matrix $\mathbf{B}$
- 251 is then decomposed via $\mathbf{B=UMV^T}$, where $\mathbf{U}$ and $\mathbf{V}$ are the orthogonal
- 252 matrices that contain the left and right singular vectors of $\mathbf{B}$. The matrix
- 253 $\mathbf{M}$ is a square matrix that contains the singular values of $\mathbf{B}$. These
- 254 singular values are placed in a decreasing order along the main diagonal
- 255 of $\mathbf{M}$. The rationale behind the application of the SVD filter is that large
- 256 singular values are typically related to dominant periodic patterns
- 257 arising from the repetitive reflections between the tree layers [18]. Thus,
- 258 setting the dominant singular values to zero and subsequently
- 259 reconstructing the matrix $\mathbf{B}$ will result to a revised B-Scan with a lower
- 260 number of features associated with ringing noise [18]. The number of
- 261 dominant singular values to be filtered out is usually <10. This number is
- 262 a hyperparameter that it is tuned via a trial and error procedure.

263   The above processing pipeline is tested in the numerical case study shown

264   in Figure 2. A generic hardwood consisted with four layers is simulated

265   using the finite-difference time domain (FDTD) method [34], [35], [36]

266   (more details on the numerical simulations are given in Section 3). An early

267   decay is simulated as a hollow chamber within the sapwood. The raw and

268   the processed data are shown in Figure 3. The static components and the

269   signal prior to time-zero are initially removed. Subsequently, a linear gain is

270   applied to each A-Scan. Lastly, an SVD filter, filtering out the three most

271   dominant eigenvalues, is applied to the data. From Figure 3, it is apparent

272   that the employed processing approach [18] can effectively remove the

273   ringing noise and can enhance the reflections from the early decay.
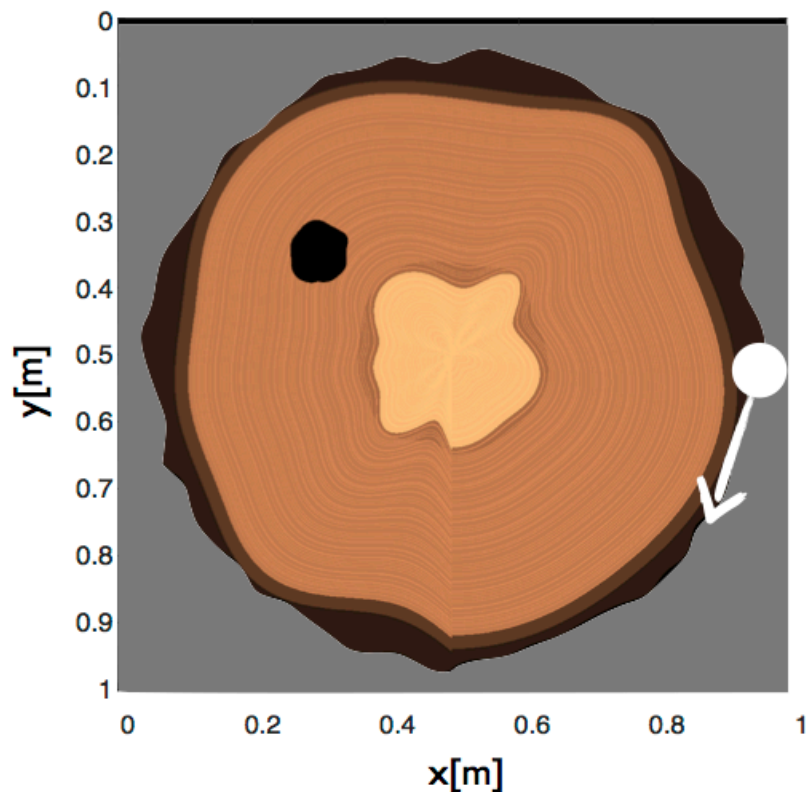
274

275 **Figure 2: A numerical case study for the investigation of the received signal of an early decay in a**
276 **generic hardwood scenario. The white dot represents the starting point of the scan and the arrow**
277 **shows the direction of the measurements.**

278

279

280
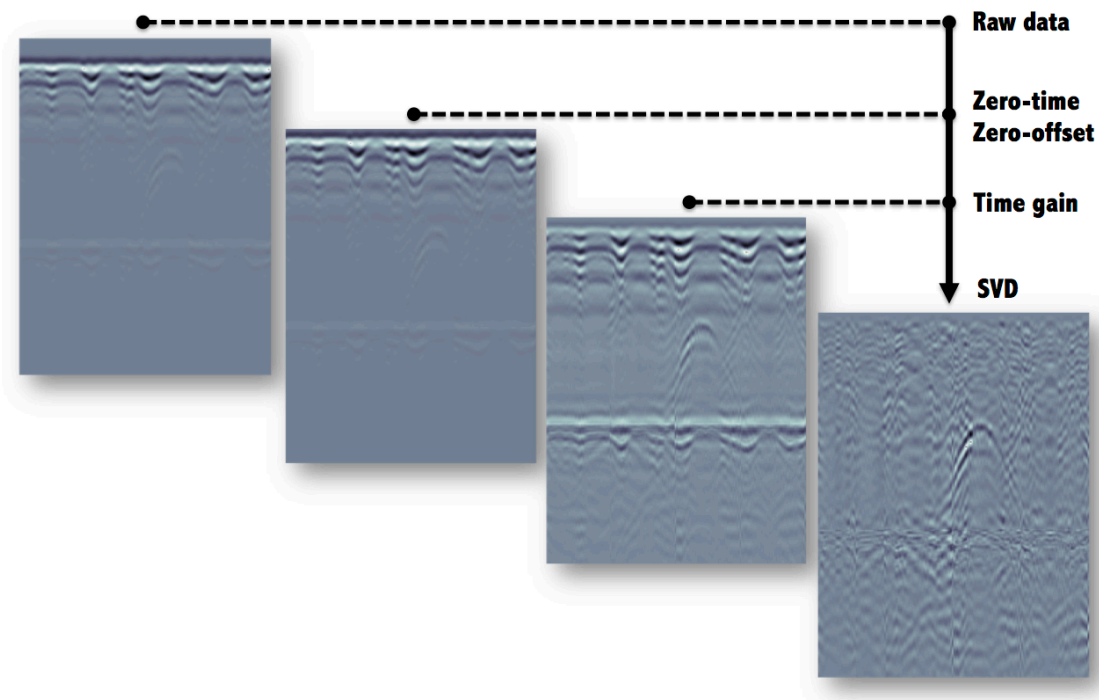
Figure 3: The employed processing pipeline applied to the simulated data from the case study illustrated in Figure 2.

283

2.3 Reverse Time Migration

RT migration using monostatic measurement configurations is based on the exploding reflector model [30]. This model approximates every scatterer with an equivalent source that is excited when the incident wave reaches the investigated target. The equivalent sources radiate towards the position of the antenna following the same path as the incident field [30]. Thus, reversing the received signals with respect to time and use them as excitation sources along **F** will result to a radiated electromagnetic field collapsing at the coordinates of the scatterers as time approaches to zero. To compensate the two-way travel time, the velocity of the medium during the back-propagation is set to half the actual velocity [30]. The mathematical formulation for the RT migration in homogenous media is

$$E_s(\mathbf{r}_m, \omega) = k_b^2 \int_0^M g_e\left(\mathbf{r}_m, \mathbf{F}(s), \omega\right) E_{inc}(\mathbf{F}(s), \omega) ds$$

296
(2)

297 where E_s is the back-propagated field in the frequency domain, $\mathbf{r}_m$ is the

298 parameter indicating the coordinates within the trunk, ω is the angular velocity,

299 k_b is the wavenumber assuming a homogenous velocity (half of the actual

300 velocity), E_{inc} is the reversed received signal after processing, M is the

301 circumference of the trunk and g_e is the Green's function for a homogenous space.

302 The Green's function in the frequency domain equals with

$$g_e\left(\mathbf{r}_m, \mathbf{F}(s), \omega\right) = \frac{j}{4} H_0^2\left(k_b||\mathbf{r}_m - \mathbf{F}(s)||\right)$$

303
(3)

304 where $j = \sqrt{-1}$ and H_0^2 is the Hankel function of the second kind and zero order

305 [24]. The migrated image is estimated after applying the inverse Fourier

306 transform to E_s and subsequently set $t = 0$.

307 It should be noted that the exploding model on which migration is based on,

308 does not take into account the presence of repetitive reflections between the tree

309 layers. Therefore, a non-adequate elimination of the ringing noise will result to

310 shallow artefacts due to the misinterpretation of the ringing noise as fictitious

311 scatterers.

312

313 *2.4 Post-migration processing*

314 The post-migrated image is subsequently subjected to image processing in

315 order to remove migration effects and enhance the quality of the signal. The

316 resulting migrated image is initially squared and subsequently convolved with a

317 2D homogenous Gaussian function

$$G(x,y) = \frac{1}{2\pi\sigma^2} e^{-\frac{x^2+y^2}{2\sigma^2}}$$

318

(4)

319 where σ is a unit-less variable that controls the intensity of the filter [37].

320
321 **Table 1: The extended Debye properties of the tree layers used for the numerical simulations [17].**

Tree Section Component	Water Content [%]	ε_∞	$\Delta\varepsilon$	σ [W⁻¹m⁻¹]	t_0 (psec)
Cambium layer	70	9	43	1	9.23
Outer sapwood	30	6.1	12.36	0.033	9.23
Inner sapwood	25	5.9	9.66	0.02	9.23
Rings	10	5.4	3.1	0.0083	9.23
Heartwood	5	5.22	1.43	0.005	9.23
Bark	0	5	0	0	9.23

322
323
324
325
326

3. Case Studies and Results

328

329 *3.1 Numerical Case Study*

330   In the current section, the proposed detection framework is tested using

331 synthetic but nonetheless realistic data. An FDTD method is used for the

332 simulations with a second order accuracy in both space and time [34], [35], [36].

333 The spatial discretisation step is set to $\Delta x = \Delta y = \Delta z = 1$ mm and the time

334 increment is chosen based on the Courant limit [34]. Regarding the excitation of

335 the system, a numerical equivalent of the commercial antenna GSSI 1.5 GHz [33]

336 is used for the simulations. Simulating the antenna in different positions along

337 the curved surface of the trunk requires the implementation of tilted excitation

338 sources. These scenarios give rise to numerical errors and instabilities due to the

339 constraints from the orthogonal grid of FDTD. To overcome this, instead of

340 moving the antenna along the trunk, the trunk is rotated while the transducer

341 remains still [18].

342   The numerical case study examined in this Section is a generic semi-saturated

343   hardwood. The simulated trunk consists of five distinct layers i.e. the bark, the

344   cambium layer, the outer-sapwood, the inner-sapwood and the heartwood. The

345   dielectric properties of the layers are estimated using a complex-refractive index

346   model (CRIM) [18] subject to the volumetric fraction of water expected in each

347   layer [18]. Subsequently, in order for the dielectric properties to be compatible

348   with FDTD, the complex permittivity is approximated with an extended Debye

349   model (see Table 1) [18], [38].   Lastly, two decays with different sizes are

350   incorporated within the outer-sapwood (see Figure 4). The decays are simulated

351   as hollow semi-cylindrical objects with their main axis being parallel to the main

352   axis of the trunk.

353   The raw B-Scan is initially subjected to the pre-processing pipeline described in

354   Section 2.2. Subsequently, the revised traces are reversed with respect to time

355   and used as input sources in equation (2). The bulk permittivity of the medium is

356   set to $\varepsilon=16$. The migrated image is then squared and subsequently smoothed

357   using a Gaussian filter (kernel size equals to 30 and σ = 15). Figure 5 illustrates

358   the migrated image and the post-migration processing steps. Moreover, Figure 6

359   shows the effect of σ on the final outputs. Increasing σ results to a low-pass filter

360   that decreases migration artefacts and high frequency noise. Both of the decays

361   are accurately detected indicating the validity of the suggested methodology.

362   From Figure 5 is apparent that the relative size between the decays can be

363   extracted from the reconstructed image. Evidences are also given regarding the

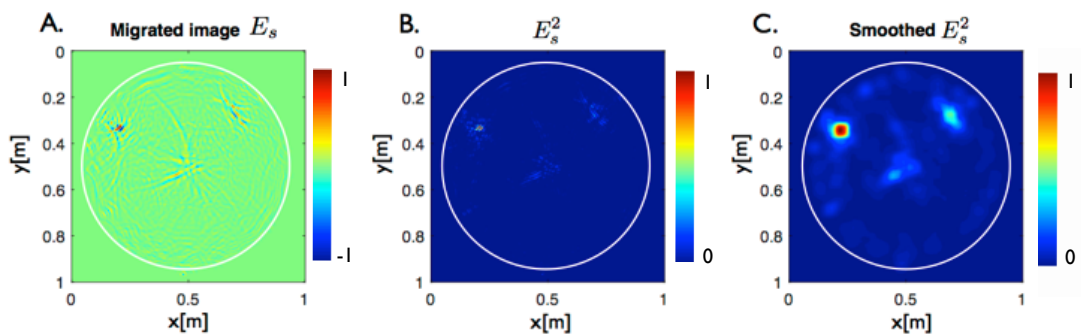364   presence of heartwood at the centre of the trunk.

365

366

367
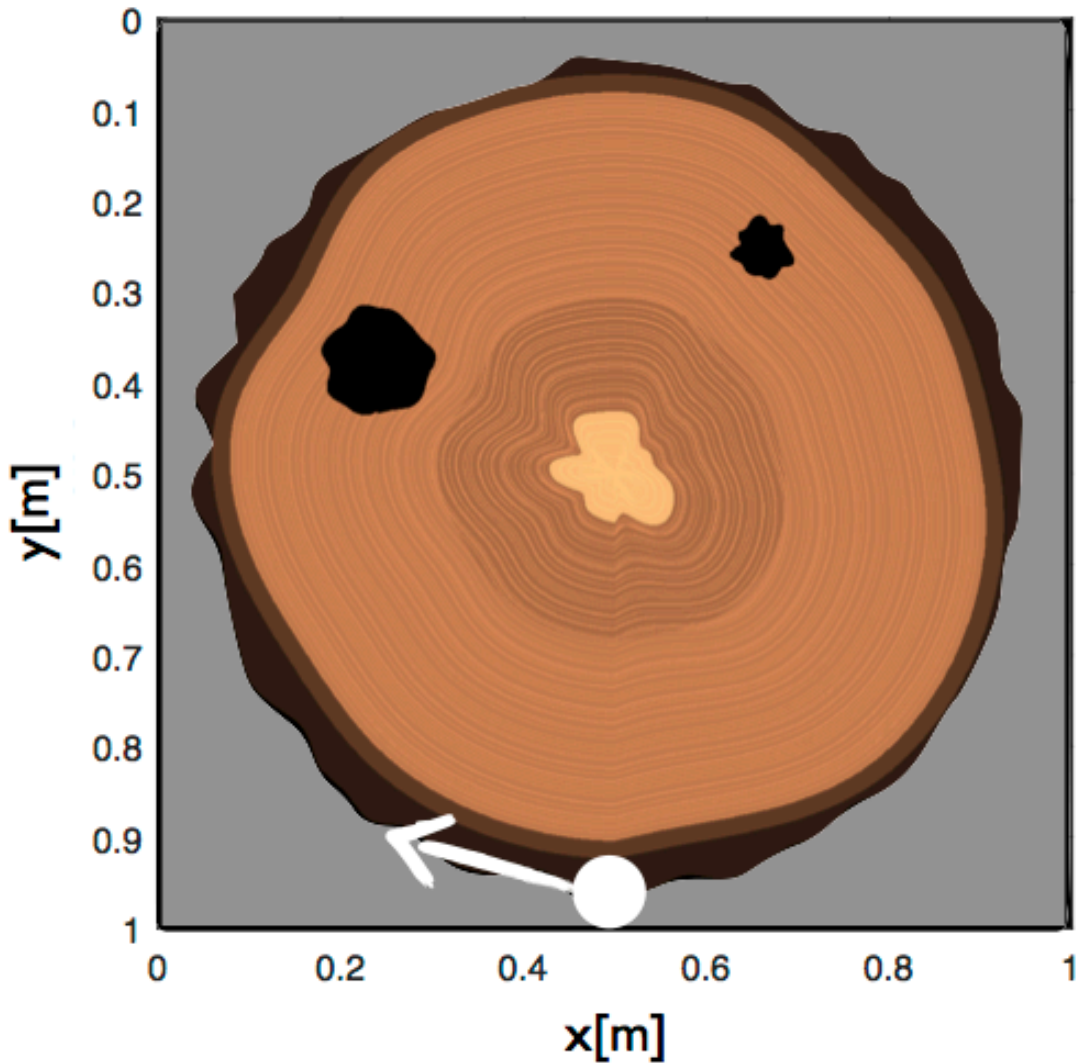
Figure 4: A numerical case study for the investigation of the received signal of two early decays in a generic hardwood scenario. The white dot represents the starting point of the scan and the arrow shows the direction of the measurements.

371

Figure 5: The reconstructed internal structure of the synthetic trunk shown in Figure 4.A) The resulting image using RT migration. B) Squaring the migrated image in order to increase the overall signal-to-clutter ratio. C) A Gaussian blur filter is applied in order to remove the migration-effects. The line of measurements is assumed circular to make the case study more realistic and challenging.
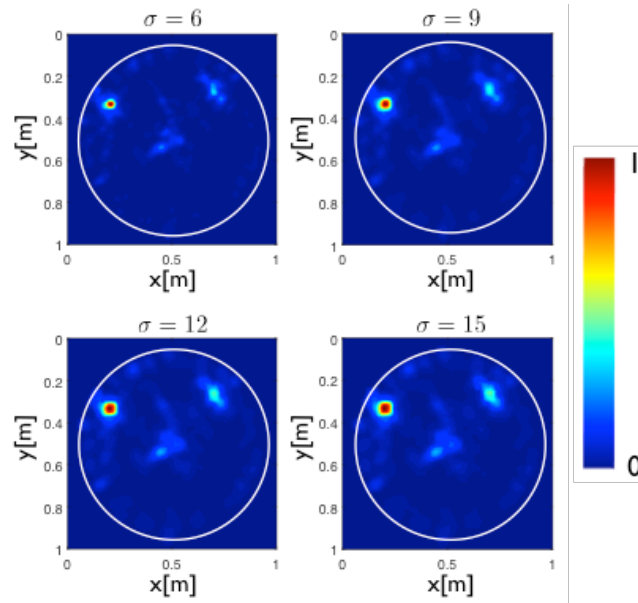
Figure 6: The effect of σ to the resulting reconstructed image. Increasing σ results to low pass filter that filters out high frequency noise and migration artefacts.

3.1 Field Measurements

The proposed detection scheme is now tested in a real-field case study from a diseased tree located at Gunnersbury Park, London, UK (see Figure 7). The employed antenna for this experiment was the dual-polarised hand-held antenna "Aladdin" from IDS GeoRadar (Part of Hexagon). The central frequency of "Aladdin" is 2 GHz, the time-step equals to $dt = 6.25e{-}11$ s and the spatial step of the measuring wheel is Δ = 1 cm. Circular scans were collected every 5 cm along the main axis of the tree and parallel to the ground. The overall scanned area is 1.35 m long and consists of 27 parallel circular scans. The inspected area has a semi-cylindrical shape with a varying circumference. The circumference of each section was accurately estimated and subsequently incorporated into the detection scheme by means of the measuring-wheel device attached to the antenna.

Prior to the measurements, the bulk permittivity of the trunk was estimated at $\epsilon \approx 30$. The permittivity was calculated based on the two-way travel time

395   needed for the wave to travel from one side of the trunk to the other. The

396   permittivity measurements were conducted using the 1 GHz horn antenna

397   system from IDS GeoRadar (Part of Hexagon). The high-directivity of the horn

398   antenna made it possible to get a clear reflection from the back of the trunk. To

399   further enhance the signal, a perfect conducting (PEC) sheet was attached to the

400   tree.

401   After the completion of the measurements, the tree was torn down (see Figure

402   8) and cut into several slices in an effort to get an insight of its internal structure.

403   From Figure 9, a dominant decay extending along the main axis of the trunk is

404   clearly visible. The decay has an irregular shape and a sharp transition from the

405   healthy sapwood. The diameter of the decay is approximately ~60 cm and does

406   not show any dominant increasing or decreasing trend along the trunk.

407   Figure 10 illustrates the reconstructed image using the methodology described

408   in Section 2. Every B-Scan is initially processed using a time-zero correction, a

409   zero-offset removal, a linear gain and an SVD filter (five dominant eigenvalues

410   are filtered out). Subsequently, an RT migration is applied to each processed B-

411   Scan subject to a homogenous medium with $\epsilon = 30$. The migrated images are

412   furthermore squared and smoothed using a Gaussian blur filter (kernel size

413   equals to 30 and σ = 15). The resulting 2D images are then combined to create

414   a pseudo-3D model of the trunk. From Figure 10, it is apparent that there are

415   clear evidences of a major feature at the centre of the trunk extending along its

416   main axis. This is in good agreement with the actual structure of the tree, shown

417   in Figure 9. A reconstructed slice of the tree and its corresponding processed B-

418   Scan are shown in Figure 11. The shape and the size of the decay are adequately

419 recovered. Discrepancies between the actual and the predicted shape are due to

420 local variations of permittivity within the trunk that deviate from the assumption

421 of a homogenous medium with $\varepsilon=30$.

422
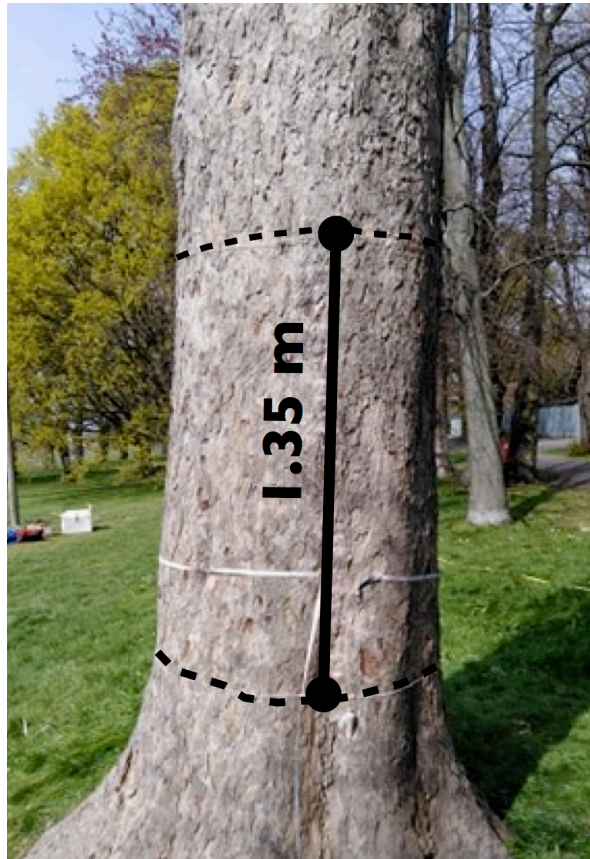
423
424 **Figure 7: The investigated tree at Gunnersbury Park, London, UK. The scanned area is highlighted between the dotted lines.**
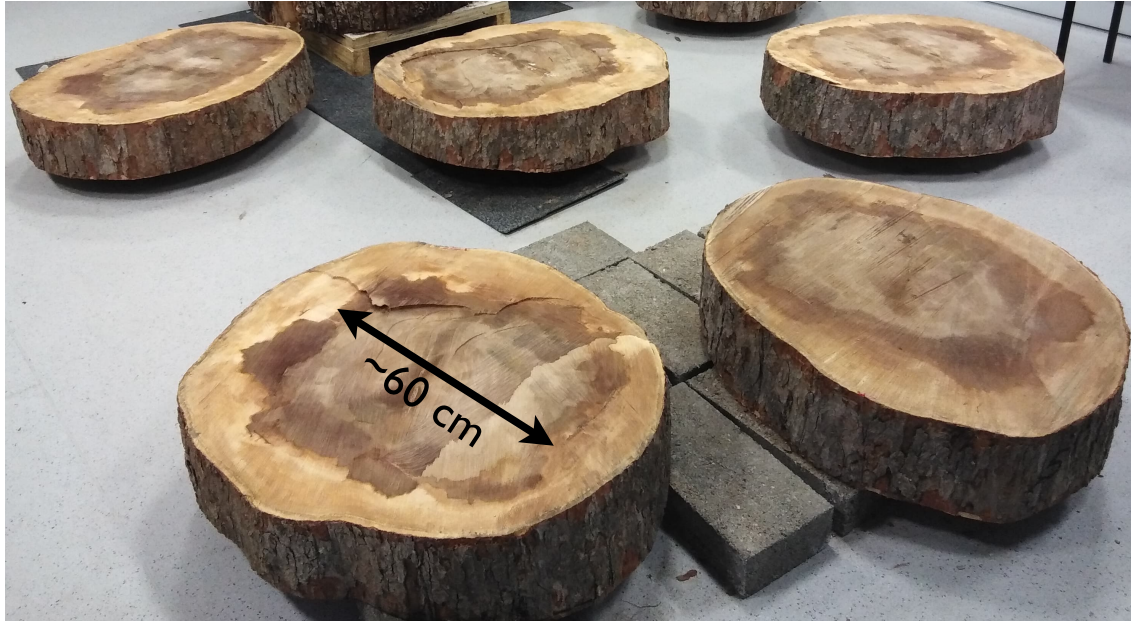
425

426
427
428 **Figure 8: The investigated tree was torn down after the completion of the measurements in order to get an insight on its internal structure.**

430

Figure 9: Slices collected from the investigated tree shown in Figure 7. A dominant decay (with a diameter of approximately ~60 cm) extending along the main axis of the trunk is clearly visible.
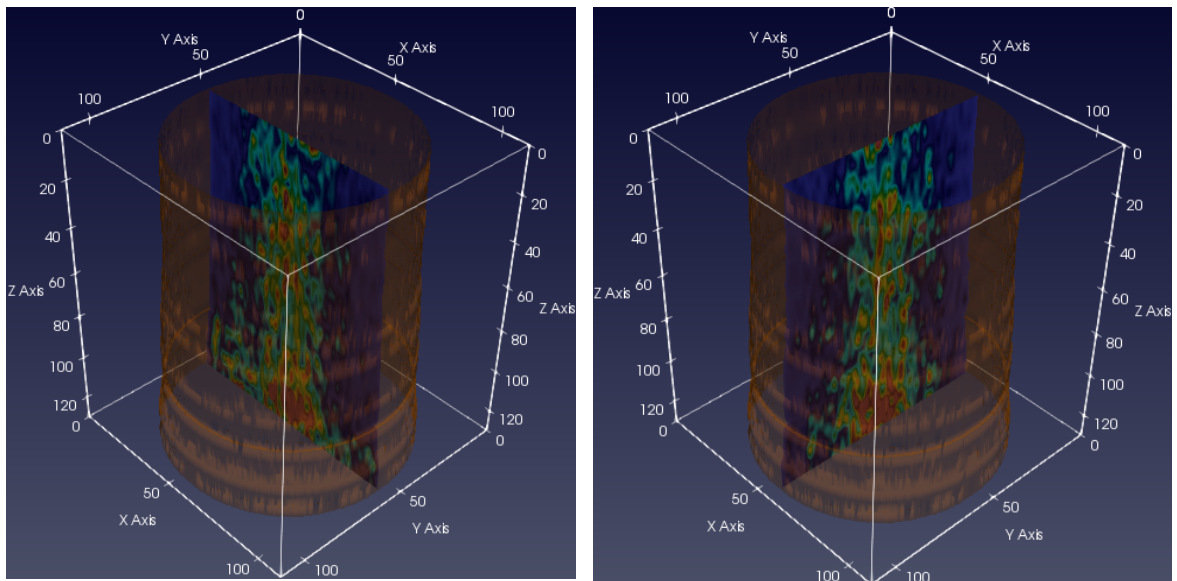
Figure 10: The reconstructed internal structure of the scanned area shown in Figure 7 using the processing scheme discussed in Section 2. The axis are in cm.

448
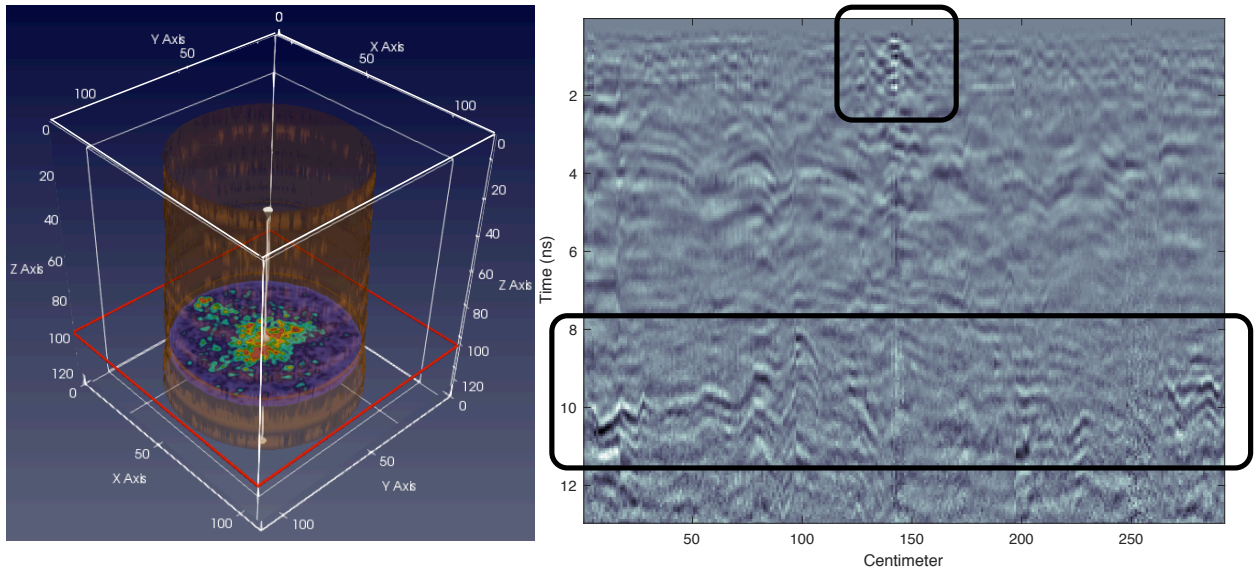
Figure 11: A reconstructed slice (left) and its corresponding processed B-Scan (right). Two main decay are apparent, one shallow with small size and one bigger one at the centre of the trunk. The reflections of the two decay are highlighted within the black boxes.

4. Conclusions

In this paper, a detection framework is described fine-tuned for detecting hidden decay and cavities in diseased trees. The main advantage of the described methodology is that it can be applied in a straightforward manner using commercial ground-penetrating radar (GPR) antennas without the need for bespoke systems and complex measurement configurations. The processing pipeline of the scheme primarily consists of a singular value decomposition (SVD) filter coupled with a reverse-time (RT) migration. This implies that the suggested methodology has minimum computational and operational requirements making it particularly appealing for large-scale forestry applications. The accuracy of the described framework is rigorously tested via numerical and real-field case studies. The results clearly suggest that GPR coupled with the proposed methodology is a robust detection tool capable of assessing the health conditions of trees in an efficient and practical manner.

468 Consequently, GPR can answer the on-going call for efficient arboriculture tools

469 and provide a viable alternative for tackling modern challenges related to

470 emerging infectious diseases of trees. The proposed methodology has been

471 validated using high frequency hand-held antennas. Future work will include the

472 application of lower frequencies in an attempt to increase the penetration depth

473 and the overall signal to clutter ratio. Lower frequency antennas are essential in

474 order to overcome the electromagnetic losses within the trunk and can

475 potentially increase the performance of the proposed methodology.

476
477

490
491
492
493

References

[1] A. Broome, D. Ray, R. Mitchell and R. Harmer, "Responding to ash dieback (Hymenoscyphus fraxineus) in the UK: woodland composition and replacement tree species," *Forestry, An International Journal of Forest Research*, vol. 92, pp. 108–119, 2019.

[2] A. Santini, L. Ghelardini, C. De Pace, [...] and J. Stenlid, "Biogeographical patterns and determinants of invasion by forest pathogens in Europe," *New Phytologist*, vol. 197, pp. 238-250, 2012.

[3] A. M. Ellison, M. S. Bank, B. D. Clinton, [...] and J. R. Webster, "Loss of foundation species: consequences for the structure and dynamics of forested ecosystem," *The Ecological Society of America*, vol. 3, pp. 479-486, 2005.

[4] S. A. Anagnostakis, "Chestnut blight: the classical problem of an introduced pathogen," *Mycologia*, vol. 79, pp. 23-37, 1987.

[5] Q. Guo, M. Rejmanek and J. Wen, "Geographical, socioeconomic and ecological determinants of exotic plant naturalization in the United States: insights and updates from improved data," *NeoBiota*, vol. 12, pp. 41-55, 2012.

[6] J. J. Stocks, R. J. A. Buggs and S. J. Lee, "A first assessment of Fraxinus excelsion (common ash) susceptibility to Hymenoscyphus fraxineus (ash dieback) throughout the British Isles," Nature, Scientific Reports, vol. 7, 2017.

[7] R. Worrell, "An Assessment of the Potential Impacts of Ash Dieback in Scotland," Available online: https: //bit.ly/2ZkYhNc (accessed on 30 August 2019)

[8] N. Brown, "Epidemiology of Acute Oak Decline in Great Britain," Available online: https://spiral.imperial.ac. uk/handle/10044/1/30827 (accessed on 30 August 2019).

[9] S. Denman, N. Brown, S. Kirk, M. Jeger and J. Webber, "A description of the symptoms of Acute Oak Decline in Britain and a comparative review on causes of similar disorders on oak in Europe," *Forestry*, vol. 87, pp. 535-551, 2014.

[10] A. M. Ellison, M. S. Bank, B. D. Clinton, [...] and J. R. Webster, "Loss of foundation species: consequences for the structure and dynamics of forested ecosystem," *The Ecological Society of America*, vol. 3, pp. 479-486, 2005.

[11] W. C. Shortle and K. R. Dudzik, *Wood Decay in Living and Dead Trees: A Pictorial Overview*, U.S. FOREST SERVICE, 2012.

[12] P.M.W.Xu and R.Wimmer,"Application of a drill resistance technique for density profile measurement in wood composite panels," *Forest Prod. J.*, vol. 45, pp. 90-93, 1995.

[13] W. Moore, "The combined use of the RESISTOGRAPH and the Shigometer for the accurate mapping and diagnosis of the internal condition of wood support orangs of trees," *Arboricultural J.*, vol. 23, pp. 273–287, 1999.

[14] V.Bucur. *Nondestructive Characterization and Imaging of Wood*. Berlin, Germany: Springer, 2003.

[15] Lantini, L., Holleworth, R., Egyir, D., Giannakis, I., Tosti, F., and Alani, A.M. (2018). Use of Ground Penetrating Radar for Assessing Interconnections between Root Systems of

Different Matured Tree Species. In: Proc of the IEEE International Conference on Metrology for Archaeology and Cultural Heritage (MetroArchaeo 2018), Cassino, Italy, October 22-24, 2018.

[16] A. Guyot, K.T. Ostergaard, M. Lenkopane, J. Fanand, D.A. Lockington, "Using electrical resistivity tomography to differentiate sapwood from heartwood: application to conifers," *Tree Physiology*, vol. 33, pp. 187– 194, 2013.

[17] C. J. Lin and T. H. Yang, "Detection of acoustic velocity and electrical resistance tomographies for evaluation of peripheral-inner wood demarcation in urban royal palms," *Urban Forestry and Urban Greening*, vol. 14, pp. 583-589, 2015.

[18] I. Giannakis, G. Tosti, L. Lantini and A. Alani, "Health monitoring of tree-trunks using ground penetrating radar," *IEEE Transactions on Geoscience and Remote Sensing,* vol. 57, no. 10, pp. 8317-8326, 2019.

[19] J. Jezova, L. Mertens and S. Lambot, "Ground-penetrating radar for observing tree trunks and other cylindrical objects," *Construction and Building Materials*, vol. 123, pp. 214– 225, 2016.

[20] J. Jezova, J. Harou and S. Lambot, "Reflection waveforms occurring in bistatic radar testing of columns and tree trunks," *Construction and Building Materials,* vol. 174, pp. 388-400, 2018.

[21] X. Xiao, J. Wen, Z. Xiao and W. Li, "Detecting and measuring internal anomalies in tree trunks using radar data for layer identification," *Journal of Sensors*, vol. 2018, pp. 1-11, 2018.

[22] G. Leucci, N. Masini, R. Persico and F. Soldovieri, "GPR and sonic tomography for structural restoration: The case of the cathedral of Tricarico," *J. Geophys. Eng.* vol. *8,* pp. S76–S92, 2011.

[23] M. Pastorino, *Microwave Imaging*, John Wiley & Sons, Inc.: Hoboken, NJ, USA, 2010.

[24] A. M. Alani, F. Soldovieri, I. Catapano, I. Giannakis, G. Gennarelli, L. Lantini, G. Ludeno and F. Tosti, "The Use of Ground Penetrating Radar and Microwave Tomography for the Detection of Decay and Cavities in Tree Trunks," *Remote Sensing*, 2019.

[25] D. J. Daniels, *Ground* Penetrating *Radar*, 2nd ed. London, U.K.: Institution of Engineering and Technology, 2004.

[26] J. Schofield, D. Daniels and P. Hammerton, "A Multiple Migration and Stacking Algorithm Designed for Land Mine Detection," *IEEE Transactions on Geoscience and Remote Sensing,* vol. 52, no. 11, pp. 6983-6988, 2014.

[27] M. A. Gonzlez-Huici, I. Catapano and F. Soldovieri, "A Comparative Study of GPR Reconstruction Approaches for Landmine Detection," *IEEE Journal of Selected Topics in Applied Earth Observations and Remote Sensing*, vol. 7, no. 12, pp. 4869-4878, 2014

[28] X. Feng, M. Sato, C. Liu and Y. Zhang, "Profiling the Rough Surface by Migration," *IEEE Geoscience and Remote Sensing Letters*, vol. 6, no.2, pp. 258-262, April 2009.

574 [29] I. Giannakis, F. Tosti, L. Lantini, D. Egyir and A. M. Alani, "Signal Processing For
575 Tree-Trunk Investigation Using Ground Penetrating Radar," in *Proc. Of 10th Workshop on*
576 *Advanced Ground Penetrating Radar,* Netherlands, 2019.

577 [30] C. J. Leuschen and R. G. Plumb, "A matched-filter-based reverse-time migration
578 algorithm for ground-penetrating radar data," *IEEE Transactions on Geoscience and Remote*
579 *Sensing*, vol. 39, no. 5, pp. 929-936, 2001.
580

581 [31] R. J. Sharpe and R. W. Thorne, "Numerical method for extracting an arc length
582 parameterization from parametric curves," *Comput.-Aided Des.,* vol. 14, no. 2, pp. 79–81,
583 1982.

584 [32] B. Guenter and R. Parent, "Computing the arc length of parametric curves," *IEEE*
585 *Comput. Graph. Appl.*, vol. 10, no. 3, pp. 72–78, 1990.

586 [33] I. Giannakis, A. Giannopoulos, and C. Warren, "Realistic FDTD GPR antenna models
587 optimized using a novel linear/nonlinear full- waveform inversion," *IEEE Trans. Geosci.*
588 *Remote Sens.*, vol. 57, no. 3, pp. 1768-1778, Mar. 2019.

589 [34] A. Taflove and S. C. Hagness, *Computational Electrodynamics: The Finite-Difference*
590 *Time-Domain Method*, 2nd ed. Norwood, MA, USA: Artech House, 2000.

591 [35] C. Warren, A. Giannopoulos, and I. Giannakis, "gprMax: Open source software to
592 simulate electromagnetic wave propagation for ground penetrating radar," *Comput. Phys.*
593 *Commun.*, vol. 209, pp. 163–170, Dec. 2016.

594 [36] C. Warren *et al.*, "A CUDA-based GPU engine for gprMax: Open source FDTD
595 electromagnetic simulation software," *Comput. Phys. Commun.*, vol. 237, pp. 208-218, Apr.
596 2019.

597 [37] S. M, Nixon and A. S. Aguado. *Feature Extraction and Image Processing for Computer*
598 *Vision*. Academic Press, 2008.

599 [38] D. F. Kelley, T. J. Destan, and R. J. Luebbers, "Debye function expansions of complex
600 permittivity using a hybrid particle swarm-least squares optimization approach," *IEEE Trans.*
601 *Antennas Propag.*, vol. 55, no. 7, pp. 1999–2005, 2007.

602

603

604

605

606

607

608

609